An Immersed Boundary Formulation for Lattice Boltzmann Simulations of low-Reynolds fluid-structure interaction problems

A. Trotta,[1], S. Meloni,[1], G. Falcucci[2], S. Ubertini,[1] and A. L. Facci[1]
[1]*Department of Economy, Engineering, Society, and Business Organisation, University of Tuscia, 01100 Viterbo, Italy and*
[2]*Department of Enterprise Engineering Mario Lucertini,*
University of Rome Tor Vergata, Via del Politecnico 1, 00133 Rome, Italy

(Dated: February 24, 2025)

Fluid-solid interaction problems are encountered in various natural phenomena and engineering applications. Specifically, when the fluid passes through a solid body, the resultant oscillatory forces may induce the structure to vibrate. In this work, the Immersed Boundary formulation has been implemented in the Lattice Boltzmann approach to study complex fluid-structure interaction problems in a two-dimensional domain. The Immersed Boundary method has been used for its capability to describe complex geometries on a separate grid with respect to the one used to solve the fluid motion: a Eulerian one, fixed in the space, for the fluid domain, and a Lagrangian one, which can move freely in the space to describe the body motion. The main advantage of using Immersed Boundary is the possibility to simulate the presence of a body through forces applied to the fluid domain, defining a discrete delta function necessary to distribute such forces. The presented approach has been applied to different Reynolds numbers flow conditions ranging from 20 up to 200 and different geometries starting from a plain cylinder. The validation results from the cylinder test case demonstrated excellent agreement with the literature, particularly in terms of Drag and Lift coefficients and the Strouhal number. The proposed algorithm captures significant high-frequency contributions arising from the interaction between vortices in the wake. Applications to both the cylinder-plate configuration and vibrating cylinder cases confirmed that this approach based on the weak fluid-structure interaction coupling can be effectively applied to a wide range of low Reynolds scenarios.

I. INTRODUCTION

Fluid-Structure Interaction (FSI) of bluff bodies is common in both natural and industrial settings, with examples ranging from the oscillations of plants in wind or water streams to vibrations in engineering structures, such as heat exchanger tubes, chimney stacks, spar hulls, cables, and mooring lines. In particular, FSI presents a significant challenge in many engineering applications, as flow-induced forces can impact the structural integrity. These interactions often result in oscillations, vibrations, and structural displacements. Specifically, FSI occurs in devices designed for energy harvesting, where fluid flow induces a mechanical motion and generates power [1–3], or in submarine communication cables, which can experience vortex-induced vibrations due to underwater currents [4, 5]. FSI phenomena can also be observed in the sedimentation of particles [6] or in the complex field of the aerodynamics [7, 8]. In this framework, it is worth noting the work of He at al., in [9] they studied the FSI problem of an airfoil with actively controlled flexible leeward using piezoelectric macro-fiber composite (MFC) actuators to enhance Lift and reduce Drag.

FSI plays an important role also in marine biology with implications in the engineering field, indeed in [10–12] Falcucci et al. studied Deep-sea glass sponges focusing on the helical skeletal structure which is able not only to reduce the overall hydrodynamic stress but also to promote an organized vertical flow within its body cavity. Moreover, interaction of buoyant rigid bodies with free surface flows attracted the interest of researchers in order to predict hydrodynamic loads, crucial for design and longevity of the structures [13, 14].

Furthermore, several research works report relevant FSI applications in the biomechanics field [15–17], where the interaction between flowing blood and arterial walls can impact both fluid behavior and vessel mechanics. The study of such interactions is critical in predicting and managing the effects of these forces.

A direct consequence of FSI is the Vortex-induced vibration (VIV), where the fluid flow around a structure generates alternating vortex shedding, leading to oscillations. VIV has been extensively studied by numerous researchers across various engineering fields, employing both numerical simulations and experimental approaches, to both reduce and enhance the effects of the vortex shedding. Mitigating the effects of VIV is crucial across various engineering fields, from civil structures to ocean engineering; significant efforts have been devoted to suppressing structural oscillations. On the other hand, for energy harvesting applications, the vibration and displacement of devices are essential, as they increase the potential for generating energy. Maximizing these movements can improve the efficiency and effectiveness of energy capture from dynamic systems. These motivations have spurred strong research interest in coupling FSI problems with VIV issues, motivations that also underpin the present work.

Over the years, various parameters and configurations have been explored, often through fundamental test cases. For example, the study in [18] delves into the effect of the gap between a cylinder and a wall to suppress vortex shedding. Additionally, the influence of flow-induced vibrations on the system's output voltage was experimentally investigated by Zhang and Wang in [19], utilizing a circular cylinder with two attached piezoelectric beams and an upstream cylinder. Numerical simulations and experiments to explore methods for the vortex shedding suppression using jets in various configurations have been presented in [20–22], focusing the analysis on mitigating the effects of VIV through active flow control techniques. Zhu et al. [5] further investigated VIV phenomena with a focus on energy harvesting applications. By attaching fin-shaped strips to a smooth cylinder, they demonstrated the potential of VIV to capture hydrokinetic energy from ocean currents, delivering a potential as a renewable energy source in marine environments. From the experimental point of view, Cui et al. [23] examined how the bending stiffness of a flexible plate attached at the rear stagnation point of a circular cylinder influences the suppression of vortex-induced vibrations. Their findings offer valuable insights into passive control mechanisms that could improve the structural stability of systems subject to VIV.

The usage of rotating rods has been widely studied from different authors [24–26]. Taheri et al. [24] numerically explored the use of rotating rods in opposite directions to increase the efficiency of VIV-based energy harvesters by optimizing the rotational motion of rods to induce greater vibrations, Zhu et al. [25] studied the impact of controlling rods' rotation direction on the suppression of VIV in the near wake of a circular cylinder, toshed light on the role of rod rotation in altering wake dynamics and its potential to suppress vortex shedding and reduce vibrations.

Due to the limitations and costs associated with experimental studies, such as the lack of suitable facilities, numerical simulations offer a valuable alternative for exploring these issues. Computational methods enable detailed analysis FSI and VIV in ways that may be challenging or impractical to achieve through physical experimentation.

In this context, this work provides a comprehensive investigation of FSI in flow past both a circular cylinder and a cylinder-plate configuration. The study employs the Lattice Boltzmann Method (LBM) coupled with the Immersed Boundary Method (IBM) to effectively model these interactions. Additionally, the research examines VIV of a rigid cylinder in detail.

We employ the LBM as an alternative to traditional Computational Fluid Dynamics (CFD) approaches, which typically rely on solving systems of Partial Differential Equations (PDEs). The primary advantage of LBM is its capability to discretize the computational domain into a regular grid, where fluid mechanics equations are solved through a sequence of simplified operations. LBM operates in two main steps: streaming and collision. From a computational perspective, the collision step is a localized algebraic operation, enabling efficient execution on parallel computing architectures, such as GPUs, computing clusters, and supercomputers. This intrinsic scalability allows for simultaneous updates across grid nodes without requiring complex dependencies, significantly improving computational efficiency.

Since LBM uses a mesoscopic approach to describe fluid behavior, it can capture effects that traditional continuum-based methods cannot accurately model, particularly at small scales, where molecular interactions become significant. At larger scales, however, it aligns well with traditional CFD, providing accurate and consistent results for macroscopic flow fields. [27]

In this study, the LBM is coupled with the IBM in a two-dimensional framework to capitalize on IBM's key advantage: efficiently handling complex boundaries without the need for detailed mesh generation. This coupling allows for flexible modeling of irregular and moving boundaries within a fixed grid, significantly simplifying simulations of complex geometries, where mesh updates at each iteration would otherwise be costly and time-consuming.

Compared to previous works, our approach introduces an efficient and accurate framework for two-dimensional simulations of both FSI and VIV phenomena.

Wu and Shu [28] presented an implicit method based on the solution of a linear system with the interpolation function ϕ_4^{cos} proposed by Cheng et al. [29], Cheylan et al. [30] combined the Immersed boundary formulation proposed by Gsell et al. [31] with the same interpolation function used by Wu and Shu [28]. Hu et al. [32] proposed a different formulation of the immersed boundary based on the interpolation of the populations over the boundary markers with the interpolation function ϕ_4^{IB} defined by Cheng et al. [29]. Unlike other studies, the present paper employed a novel combination of the immersed boundary method and an interpolation function, demonstrating that the interpolation function ϕ_3^{IB} proposed by Cheng et al. [29], combined with the implicit method presented by Wu and Shu [28], can accurately predict very well the forces exerted on the boundary. Additionally, our algorithm enables simulations with low computational cost while achieving high-frequency resolution. This efficiency allows us to capture high-frequency flow characteristics with remarkable accuracy, making our method ideal for preliminary simulations on a standard laptop.

For low Reynolds number applications, we employed weak fluid-structure coupling due to the significant advantages in computational efficiency and numerical stability. At low Reynolds numbers, where fluid flow typically exhibits smooth and predictable patterns, weak coupling effectively captures essential fluid-structure interactions without the complexity and computational overhead of fully coupled models.

The manuscript is organized as follows: details on the numerical approach and methodology are given in section II. The simulation validation is presented in section III; main results are reported in section IV whereas conclusions presented in section V.

II. METHODOLOGY

A. Lattice Boltzmann Method

The Lattice Boltzmann Equation (LBE) is a simplified version of Boltzmann kinetic equation, designed to simulate the dynamic behavior of fluid flows without directly solving the continuum mechanics equations. Instead, macroscopic fluid behavior arises from the streaming and collision of a conceptual ensemble of particles on a discrete space-time lattice [27, 33, 34].

By discretizing the Boltzmann kinetic equation in physical space, time and velocity space, the LBE can be written as:

$$f_i(\mathbf{x}_f+\mathbf{c}_i\Delta t, t+\Delta t) = f_i(\mathbf{x}_f,t)+\Omega_i(\mathbf{x}_f,t)\Delta t+S_i(\mathbf{x}_f,t)\Delta t, \quad (1)$$

which represents the evolution of probability density function $f_i(\mathbf{x}_f,t)$ according to their propagation along the predetermined lattice directions $\mathbf{c}_i$ and their collisions, [35].

The collision process is an algebraic local operation and is simplified in this case with the Bhatnagar–Gross–Krook (BGK) collision operator, Eq. 2, which assumes the relaxation of populations f_i towards their local equilibrium f_{eq} in a time τ [36].

$$\Omega_i = -\frac{1}{\tau}(f_i - f_{eq}) \quad (2)$$

In Eq. 1 $S_i(\mathbf{x}_f,t)$ is called source term, it is introduced in order to model internal or external forces acting on the fluid. Several forcing schemes have been proposed through the years each one with a different approach to integrate the force term [37]. The scheme chosen for the present approach is the Guo's forcing scheme [38]:

$$S_i(\mathbf{x}_f,t) = w_i\left(1-\frac{1}{2\tau}\right)\left(\frac{\mathbf{c}_i-\mathbf{u}(\mathbf{x}_f,t)}{c_s^2}+\frac{(\mathbf{c}_i\cdot\mathbf{u}(\mathbf{x}_f,t))\mathbf{c}_i}{c_s^4}\right)\cdot\mathbf{F}(\mathbf{x}_f,t), \quad (3)$$

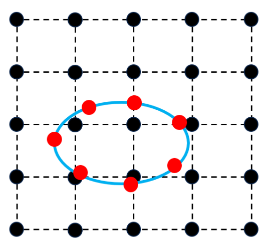

FIG. 1. Scheme of the coupling between IBM nodes (red dots) and LBM sites (black dots), cyan curve represents the obstacle's boundary

where w$_i$ are the weights of each population, c_s is the lattice speed of sound, $\mathbf{F}(\mathbf{x}_f,t)$ is the force density at the fluid node.

B. Immersed Boundary Method

To analyze complex and moving geometries the IBM has been implemented in the LBM framework.

The IBM is an approach introduced to model flows around deformable, curved and moving objects since it allows to avoid the time consuming re-meshing procedure necessary when the body conforms the fluid mesh.

Peskin [39] first introduced this method to model flows around heart valves. Feng and Michaelides [40] combined for the first time the LBM and the IBM to simulate rigid disks in 2D. In the IBM there are two set of coordinate systems, the Eulerian grid for the fluid which is stationary and the Lagrangian mesh used for the boundary of the object, see Fig. 1. Indeed, the idea of the IBM is to approximate the boundary by a set of points that affect the fluid by a force field; a force density term is then added in the flow governing equation in order to satisfy the no-slip condition on the boundary [41–43].

The IBM is also called non-body-conformal grid method, this means that the grid used to solve fluid equations does not conform to the boundary which is generated through a surface grid. The main advantage of this method is then related to the generation of the grid. Indeed, the Eulerian grid used to solve fluid equations is generated with no regard to the surface grid, its shape is not affected from the presence of the boundary.

This advantage is more apparent when moving boundaries are studied, as no re-meshing procedure is needed. This makes the IBM useful to study complex and moving or even deformable boundaries [44–46]. Since the Eulerian grid does not conform the solid boundary, it is necessary to modify fluid equations in the proximity of the boundary [47, 48].

There are different IBMs available in literature for both rigid and deformable boundaries; we can distinguish between feedback forcing methods [39], also knonw as penalty method, and direct forcing methods [49].

In this work the Direct-force Implicit IB formulation proposed by Wu and Shu in [28] is used; the diffuse interface scheme is then adopted to represent the boundary.

While in the conventional IBM the force density is evaluated in advance and then used to explicitly correct the velocity term, in the implicit formulation the magnitude of the force density is unknown and it is determined in order to satisfy the no-slip velocity condition on the boundary.

Since two different grid systems are present it is necessary couple them by introducing an interpolation stencil.

Among the interpolation functions available in the literature [29], the one chosen for the present study is:

$$\delta(r) = \begin{cases} \frac{1}{3}(1+\sqrt{1-3r^2}) & 0 \le |r| \le \frac{1}{2}\Delta x \\ \frac{1}{6}(5-3|r|-\sqrt{-2+6|r|-3r^2}) & \frac{1}{2}\Delta x \le |r| \le \frac{3}{2}\Delta x \\ 0 & \frac{3}{2}\Delta x \le |r| \end{cases} \quad (4)$$

where Δx is the lattice spacing. In the present study the interpolation function Eq. 4 has been implemented and used to compute the kernel function, Eq. 5.

$$\Delta(\mathbf{x}_f-\mathbf{X}_b^i) = \delta(x_f-X_b^i)\delta(y_f-Y_b^i), \quad (5)$$

where $\mathbf{x}_f := (x_f,y_f)$ and $\mathbf{X}_b^i := (X_b^i,Y_b^i)$ are respectively the position of the fluid node and the position of the $i-th$ Lagrangian marker.

Eq. 5 is then used to interpolate the velocity $\mathbf{u}^*(\mathbf{X}_b^i,t)$, Eq. 6, and the density $\rho(\mathbf{X}_b^i,t)$, Eq. 7, along all boundary nodes.

$$\mathbf{u}^*(\mathbf{X}_b^i,t)=\sum_{\mathbf{x}_f}\mathbf{u}(\mathbf{x}_f,t)\Delta(\mathbf{x}_f-\mathbf{X}_b^i), \tag{6}$$

$$\rho(\mathbf{X}_b^i,t)=\sum_{\mathbf{x}_f}\rho(\mathbf{x}_f,t)\Delta(\mathbf{x}_f-\mathbf{X}_b^i), \tag{7}$$

To find the force density term, a linear system should be solved Eq. 8

$$\mathbf{AQ}=\mathbf{B}, \tag{8}$$

where:

- $\mathbf{A}$ is a $P\times P$ matrix, where P is the number of Lagrangian points, whose elements are only related to the Lagrangian boundary points and their neighboring Eulerian nodes, see Eq. 9;
- $\mathbf{B}$ is the delta velocity vector between the velocity of each Lagrangian boundary node and the interpolated fluid velocity in the absence of the obstacle, see Eq. 10;
- $\mathbf{Q}$=$\left\{\delta\mathbf{u}_b^1,\delta\mathbf{u}_b^2,...,\delta\mathbf{u}_b^P\right\}$ is the velocity correction term on each Lagrangian point, see Eq. 11, and it is used to compute the force term on the boundary nodes Eq. 12.

$$\mathbf{A}(\mathbf{X}_b^i,\mathbf{X}_b^j)=\sum_{\mathbf{x}_f}\Delta(\mathbf{x}_f-\mathbf{X}_b^i)\Delta(\mathbf{x}_f-\mathbf{X}_b^j)\Delta s, \tag{9}$$

$$\mathbf{B}(\mathbf{X}_b^i)=\mathbf{U}_b(\mathbf{X}_b^i,t)-\mathbf{u}^*(\mathbf{X}_b^i,t), \tag{10}$$

where $\mathbf{U}_b(\mathbf{X}_b^i,t)$ is the wall velocity at each Lagrangian marker.

$$\mathbf{Q}=\mathbf{A}^{-1}\mathbf{B}, \tag{11}$$

$$\mathbf{F}(\mathbf{X}_b^i,t)=2\frac{\rho\,\delta\mathbf{u}_b^i}{\delta t}, \tag{12}$$

Then, the force term on each Eulerian node $\mathbf{F}(\mathbf{x}_f,t)$ is computed with Eq. 5 spreading the Lagrangian force $\mathbf{F}(\mathbf{X}_b^i,t)$, evaluated with Eq. 12:

$$\mathbf{F}(\mathbf{x}_f,t)=\sum_{\mathbf{X}_b^i}\mathbf{F}(\mathbf{X}_b^i,t)\Delta(\mathbf{x}_f-\mathbf{X}_b^i)\Delta s, \tag{13}$$

where Δs is the distance between two subsequent boundary nodes.

To evaluate the Drag and Lift forces, F_D and F_L it is sufficient using the following equations respectively Eq. 14 for the former and Eq. 15 for the latter one:

$$F_D=-\sum_{\mathbf{X}_b^i}\mathbf{F}(\mathbf{X}_b^i,t)_{\text{Streamwise}}\Delta s, \tag{14}$$

$$F_L=-\sum_{\mathbf{X}_b^i}\mathbf{F}(\mathbf{X}_b^i,t)_{\text{Spanwise}}\Delta s, \tag{15}$$

Then it is possible computing the Drag and Lift coefficients, respectively C_D and C_L, using Eqs. 16 and 17.

$$\mathrm{C_d}=\frac{F_D}{\frac{1}{2}\rho u_\infty^2 S}, \tag{16}$$

$$\mathrm{C_l}=\frac{F_L}{\frac{1}{2}\rho u_\infty^2 S}, \tag{17}$$

where ρ is the density of the fluid, u_∞ is the undisturbed speed and S is the cross section.

C. Algorithm

Figure 2 reports the algorithm developed in this work. It is possible to see how the LBM has been coupled with the IBM to manage the boundary motion. Specifically, the algorithm starts applying the boundary condition on all the boundary nodes. Then there are two ways to account for the presence of an obstacle: following the classical LBM approach with wall boundary condition, or employing the IBM.

In this paper, we employ a standard D2Q9 [50] lattice, see Fig. 3. At the inlet we fix Dirichlet boundary conditions:

$$f_{\bar{i}}(\mathbf{x}_b,t+\Delta t)=f_i^*(\mathbf{x}_b,t)-2w_i\rho_w\frac{\mathbf{c}_i\cdot\mathbf{u}_{in}}{c_s^2}, \tag{18}$$

where $f_{\bar{i}}$ refers to the direction $\bar{i}$ such that $\mathbf{c}_{\bar{i}}=-\mathbf{c}_i$, $\mathbf{x}_b$ is the boundary node, f_i^* is the distribution after collision, ρ_w is the density on the boundary nodes, $\mathbf{u}_{in}$ is the inlet velocity.

On the outlet boundary nodes the Non Equilibrium Extrapolation Method (NEEM) boundary condition has been adopted:

$$f_i(\mathbf{x}_b,t)=f_i^{eq}(\rho_w,\mathbf{u}_w)+(f_i(\mathbf{x}_f,t)-f_i^{eq}(\rho_f,\mathbf{u}_f)), \tag{19}$$

where $f_i(\mathbf{x}_b,t)$ is the population on the boundary node, $f_i(\mathbf{x}_f,t)$ is the population on the adjacent fluid node, $f_i^{eq}(\rho_w,\mathbf{u}_w)$ and $f_i^{eq}(\rho_f,\mathbf{u}_f)$ are the equilibrium distribution function evaluated respectively with the values of density and velocity of the boundary and of the last fluid node.

Near the outlet boundary an absorbing viscous sponge layer has been introduced in order to reduce reflections at the boundary. Within this layer the system is characterized by a higher viscosity than the simulation domain [51, 52]. A cubic local function for the viscosity has been implemented inside the absorbing layer. The function depends on the Reynolds number in the bulk and on the Reynolds number at the outlet. The relationship is defined as follow:

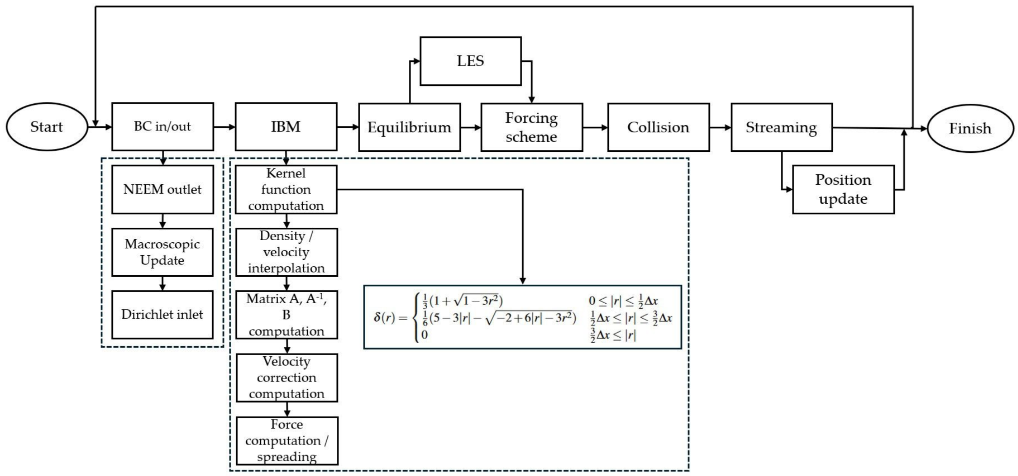

FIG. 2. A sketch of the presented algorithm.

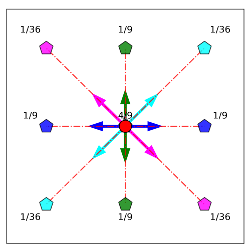

FIG. 3. Sketch of the D2Q9 stencil with weights.

$$Re(\mathbf{x}_f, Re_{in}, Re_{out}) = \begin{cases} \frac{Re_{out}-Re_{in}}{\left(\frac{Re_{in}}{2}\right)^3}\left(x_f - N_x + \frac{Re_{in}}{2}\right)^3 + Re_{in} & N_x - \frac{Re_{in}}{2} - 50 \leq x_f \leq N_x - 50 \\ Re_{out} & N_x - 50 \leq x_f \leq N_x \end{cases} \tag{20}$$

where:

- Re_{in} is the Reynolds number in the bulk;
- Re_{out} is the prescribed Reynolds number at the outlet for a desired viscosity;
- N_x is the length of the domain in the x direction.

On top and bottom boundary nodes the the free slip condition has been ensured.

The IBM algorithm starts with the computation of the kernel function Eq. 5 based on the specific interpolation function. The interpolation function chosen for this paper is Eq. 4.

Then the interpolation step of the macroscopic quantities starts, see Eqs. 6 and 7.

After that, it is necessary to compute the matrix **A** and its inverse and the vector **B**, in this way it is possible to solve the linear system, see Eq. 8, and find the delta velocity vector **Q**.

Then, the force term is computed Eq. 12 and therefore spread over the Eulerian nodes Eq. 13.

The algorithm supports turbulence modeling using a Large Eddy Simulation approach (LES) with the Smagorinsky subgrid-scale model [53]. However, since all simulations in this study are two-dimensional, and the Reynolds numbers simulated fall within the laminar flow regime, the use of the LES model has been deemed unnecessary.

Forces are then forwarded in the LBM using Guo's forcing scheme, see Eq. 3. Finally, the algorithm continues with the collision and the streaming steps.

The algorithm offers additional options for estimating the vibration of a solid structure, whether vortex-induced or not. A weakly coupled approach has been used within the framework proposed. Forces exerted on the body are evaluated with the fluid solver and passed to the Verlet algorithm [54] which is used to predict the position and the velocity of the boundary at the next time step. These information are transferred back to the fluid solver.

The body is assumed to be rigid; the position update is performed using Verlet's algorithm taking as reference position the geometrical center of the body:

$$\mathbf{X}_{ref}(t+\Delta t) = 2\mathbf{X}_{ref}(t) - \mathbf{X}_{ref}(t-\Delta t) + \mathbf{a}(t)\Delta t^2, \quad (21)$$

$$\mathbf{U}_{ref}(t+\Delta t) = \frac{\mathbf{X}_{ref}(t+\Delta t) - \mathbf{X}_{ref}(t)}{\Delta t}, \quad (22)$$

$$\mathbf{a}(t) = \frac{\mathbf{F}_{ext}(t)}{m}, \quad (23)$$

In the equations above, $\mathbf{X}_{ref}(t+\Delta t)$ is the reference position of the body at the next time step, $\mathbf{X}_{ref}(t)$ represents the reference position of the body at the time t, $\mathbf{X}_{ref}(t-\Delta t)$ is the reference position of the body at the previous time step, $\mathbf{a}(t)$ is the acceleration at time t, see Eq. 23 where $\mathbf{F}_{\text{ext}}(\text{t})$ are the forces exerted on the body and m is the mass of the rigid body, $\mathbf{U}_{ref}(t+\Delta t)$ in Eq. 22 is the velocity of the reference position at the next time step, Δt is the physical time step.

The velocity obtained in Eq. 22 is used then to update the velocity of the boundary as follow

$$\mathbf{U}_b(\mathbf{X}_b^i, t+\Delta t) = \mathbf{U}_{ref}(t+\Delta t). \quad (24)$$

The development of the position of the rigid body over time has been monitored in terms of percentage displacement $Disp_{\%}$ only along the y-direction using the following equation:

$$Disp_{\%} = \frac{X_{ref-y} - X_{ref-y0}}{D} * 100, \quad (25)$$

where X_{ref-y} is the y component of the reference position, X_{ref-y0} is the y component of the reference position at $t=0$ and L is the characteristic length.

The computational domain is set to a spanwise length of 30 cylinder diameters and a streamwise length of 40 diameters. The cylinder is fixed within the domain, with its center located 10 diameters from the inlet and 15 diameters from both the upper and lower boundaries, as illustrated in Fig. 4.

These domain dimensions ensure stable simulation while minimizing the influence of boundary conditions [28, 32, 55]. This setup strikes a balance between computational efficiency and the accuracy of results, ensuring reliable validation of the algorithm.

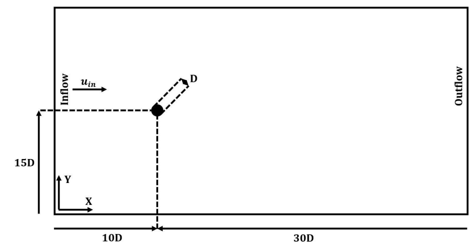

FIG. 4. Cylinder test case domain size

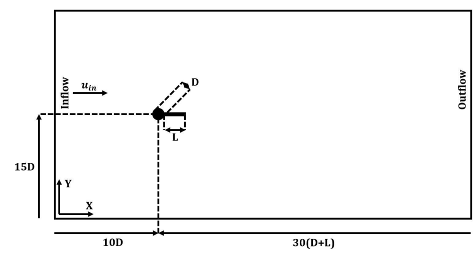

FIG. 5. Cylinder-plate domain size

The physical grid spacing used is $\mathrm{d}x = 0.001$ m; the temporal discretization parameter $\mathrm{d}t$ has been evaluated as follows:

$$\mathrm{d}t = (\tau - 0.5) * \frac{\mathrm{d}x^2}{3\nu}, \quad (26)$$

where ν is the physical viscosity of the fluid.

The domain has been discretized with 1.08 million lattice points for all the simulations which involves the cylinder configuration, while 2.16 million lattice points have been used in the cylinder with plate configuration. The temporal discretization parameter has been set to 1.023×10^{-2}[s] at Reynolds 20, 5.117×10^{-3}[s] at Reynolds 40, 2.046×10^{-3}[s] at Reynolds 100 and 1.023×10^{-3}[s] at Reynolds 200.

III. VALIDATION

The validation of the algorithm proposed in this paper is performed using a simple academic test case: flow past a stationary circular cylinder at different Reynolds numbers. In the present configuration, a range of Reynolds numbers from 20 to 200 has been tested, and the results have been compared with available data for validation purposes.

After that, the cylinder-plate configuration was examined specifically at a Reynolds number of 200. The aspect ratio of this setup is defined as $L/D = 1$ where L is the length of the plate and D is the diameter of the cylinder.

Due to the change in the streamwise dimension of the obstacle, the computational domain was resized to ensure

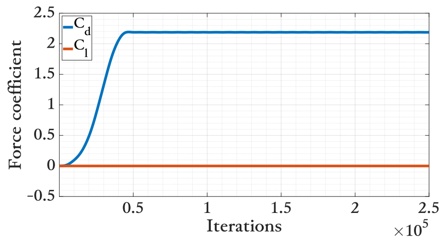

FIG. 6. Drag and Lift coefficients for circular cylinder at Re=20.

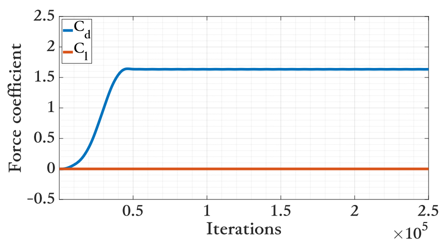

FIG. 7. Drag and Lift coefficients for circular cylinder at Re=40.

that boundary conditions did not affect the simulation results. While the spanwise dimension remained unchanged, the streamwise dimension of the domain was increased as illustrated in Fig. 5.

To comprehensively validate the numerical model, the time evolution of the Drag and Lift coefficients for a stationary cylinder at various Reynolds numbers (i.e. 20, 40, 100, and 200) is presented in Figs. 6–9.

As expected, a flat trend with no Lift is observed for the lower Reynolds cases (Figs. 6 and 7), along with a stable Drag after a transient phase lasting 50,000 iterations. No vortex shedding is expected for these cases. Increasing the Reynolds number the transient time of the simulation increases, see Figs. 8 and 9, primarily due to the instabilities introduced by vortex shedding as the flow passes around the cylinder.

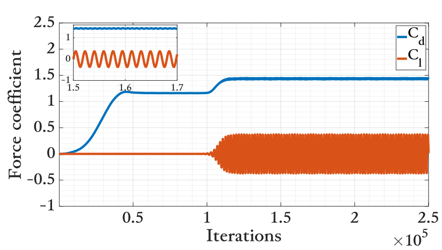

FIG. 8. Drag and Lift coefficients for circular cylinder at Re=100.

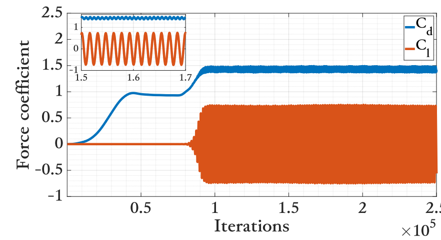

FIG. 9. Drag and Lift coefficients for circular cylinder at Re=200.

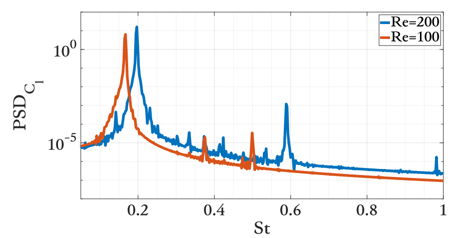

FIG. 10. PSD of C_l for cylinder configuration versus St

Furthermore, consistent with the literature, Lift and Drag begin to oscillate, with the Lift oscillating around a mean value of zero, while the Drag stabilizes an oscillatory trend around a value close to 1.5 [30, 32, 55–57].

To analyze the oscillation frequency in detail, a spectral analysis of the Lift and Drag coefficients was conducted evaluating the Power Spectral Density (PSD) using Welch's method [58, 59]. The results are presented versus Strouhal number (St) in Figs. 10 and 11. For the sake of clarity the St number has been defined as follows:

$$\mathrm{St} = \frac{\phi_0 D}{u_\infty}, \tag{27}$$

where ϕ_0 is the oscillation frequency, D is the cylinder diameter and u_∞ is the free stream flow velocity. Fig. 10 reports

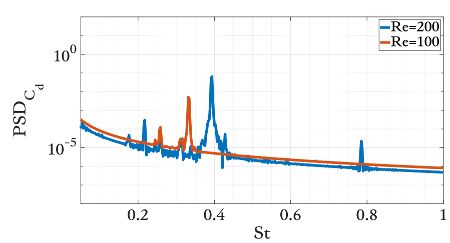

FIG. 11. PSD of C_d for cylinder configuration versus St

TABLE I. Comparison between results of the present paper and literature ones at Re=20 for the cylinder test case

Re = 20		
Reference	**Year**	**C_d**
Kang et al.[41]	2010	2.09
Niu et al.[61]	2006	2.14
He et al.[62]	1997	2.15
Present		**2.18**
Hu et al.[32]	2014	2.21
Xu et al[56].	2006	2.23

TABLE II. Comparison between results of the present paper and literature ones at Re=40 for the cylinder test case

Re = 40		
Reference	**Year**	**C_d**
He et al.[62]	1997	1.499
Kang et al.[41]	2010	1.572
Niu et al.[61]	2006	1.589
Present		**1.63**
Hu et al.[32]	2014	1.66
Xu et al[56].	2006	1.66

the PSD of the Lift coefficients for two Reynolds numbers. According to observations and the literature [30, 32, 55–57], the Von Kármán vortex shedding frequency is generally below a St number of 0.2 and increases with the Reynolds number. Additionally, at Reynolds numbers around 200, a higher harmonic with significant energy content appears at a frequency approximately three times that of the Von Kármán frequency. This phenomenon is linked to the activation of an additional flow mode, driven by nonlinearities in vortex-shedding dynamics and complex interactions between shed vortices within the wake. The detection of high harmonics of the Lift coefficient can be crucial for predicting the response of structures subjected to VIV [60].

Fig. 11 presents the PSD of the Drag coefficient as a function of the Strouhal number. As expected, the dominant frequency in this case, corresponding to the Von Kármán vortex shedding, is twice that observed for the Lift coefficient and is influenced by the Reynolds number. A secondary peak, occurring at four times the fundamental frequency, appears at a Reynolds number of 200. This peak is likely attributed to flow instability; however, its very low amplitude relative to the non-zero mean Cd value makes it negligible for VIV concerns.

C_d, C_l and St error have been computed with respect to literature data as $\varepsilon = \frac{|M-E|}{E}$ where M is the measured value, E is the expected value. Such an error is below 3% for alla considered cases, see tables I–IV. This accuracy confirms the correct computation of the forces acting on the obstacle discretized using the IBM.

TABLE III. Comparison between results of the present paper and literature ones at Re=100 for the cylinder test case

Re = 100				
Reference	**Year**	**C_d**	**C_l**	**St**
Hu et al.[32]	2014	1.418	±0.367	0.166
Cheylan et al.[30]	2022	1.42	±0.33	0.166
Xu et al[56].	2006	1.423	±0.34	0.171
Present		**1.435**	**±0.37**	**0.167**
Lai et al.[55]	2000	1.447	±0.33	0.165
Benson et al.[57]	1989	1.46	±0.38	0.17

TABLE IV. Comparison between results of the present paper and literature ones at Re=200 for the cylinder test case

Re = 200				
Reference	**Year**	**C_d**	**C_l**	**St**
Hu et al.[32]	2014	1.394	±0.712	0.195
Xu et al.[56]	2006	1.42	±0.66	0.202
Present		**1.429**	**±0.74**	**0.196**
Lai et al.[55]	2000	1.44	−	0.184
Benson et al.[57]	1989	1.45	±0.65	0.193

IV. TEST CASES

A. Cylinder-plate

The first test case analyzed is the cylinder-plate configuration at Re=200. The presence of a plate attached to the rear stagnation point of the cylinder significantly alters the vortex shedding characteristics compared to an isolated cylinder. Indeed, in the cylinder configuration vortexes are compact and the wake is symmetric respect to the horizontal line, furthermore velocity gradients between vortexes and surrounding flow are sharper respect to the one which shed from the cylinder-plate configuration.

Then, the presence of the plate behind the cylinder alters the wake structure adding complexity generating secondary structures in the wake, the regular shedding frequency typical of the cylinder case is broken, vortexes are more stretched with a lower intensity. Moreover, the plate causes a delay in the vortex shedding by modifying the flow separation points, see Fig. 12.

Drag and Lift coefficients have been monitored over time. The cylinder-plate C_d is 30% lower respect to the cylinder configuration, see table V and Fig. 13. Similarly its oscillations are smaller respect to the simple cylinder, the C_d stabilizes at a mean value around 1.1.

Similarly, the C_l amplitude is 75% lower in the cylinder-plate case respect to the simple cylinder, see Fig. 13.

This is also evidenced in the PSD of the Lift coefficient, see Fig. 14, where a reduction in both frequency and amplitude of the vortex shedding is observed. Additionally, while in the simple cylinder is clearly visible higher harmonic contribution, in the cylinder-plate configuration it disappear; instead, multiple smaller peaks are visible between St = 0.152 and St = 0.55 caused by weaker and less coherent vortices.

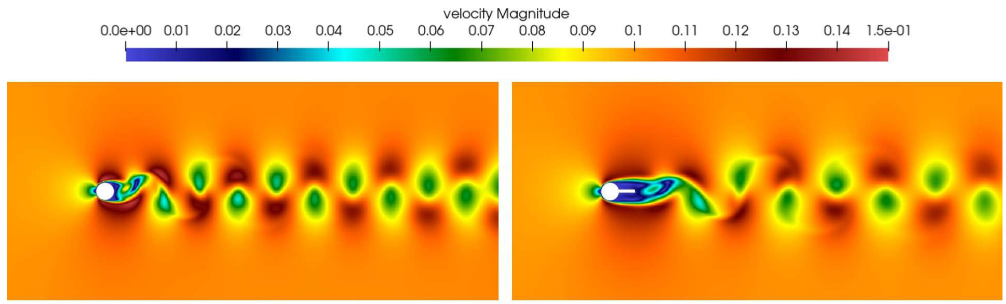

FIG. 12. Lattice velocity map at Re=200, on the left the cylinder configuration, on the right the cylinder-plate configuration

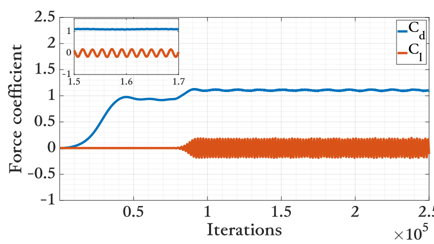

FIG. 13. Drag and Lift coefficients for cylinder-plate configuration at Re=200

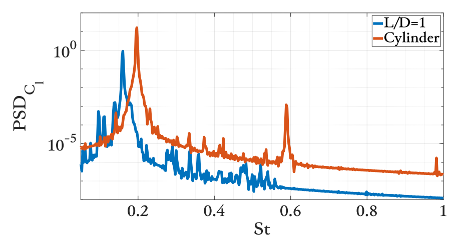

FIG. 14. PSD of the C_l of the cylinder and cylinder-plate configuration versus St

TABLE V. Comparison between cylinder (L/D=0) and cylinder-plate configuration (L/D=1) at Re=200

	Re = 200		
	$\mathbf{C_d}$	$\mathbf{C_l}$	**St**
L/D=0	1.429	±0.74	0.196
L/D=1	1.107	±0.18	0.152

FIG. 15. Model of the system

B. Vortex-Induced Vibration

VIV problem is modeled as a spring-mass system [63], as shown in Fig. 15, where the spring represents the full elasticity of the support. For this initial application, we use an aluminum disk with a mass m of 1.89×10^{-3}kg while the spring's elastic constant k is set to 1×10^{-5}N/m given the relatively small forces in this configuration. The system is restricted to a single degree of freedom along the y-axis, allowing us to consider only the Lift force and spring force to calculate the body's acceleration and resulting displacement with Eq. 25. Only the cylinder configuration exhibiting higher flow instabilities at a Reynolds number of 200 is considered. The system proposed in the present paper is characterized by a natural frequency $\phi_n = 1.16 \times 10^{-2}$Hz, defined as $\phi_n = \frac{\sqrt{\frac{k}{m}}}{2\pi}$, where k is the spring constant and m is the mass of the system.

The contribution of the high-frequency component, attributed to Lift forces, is clearly evident in Fig. 16. Additionally, a lower-amplitude, longer-period oscillation, likely associated with the natural frequency ϕ_n, is also observed. Spectral analysis of the displacement signal compared with the Lift coefficient and the analytical displacement evaluated as follow:

$$\mathbf{X}_{ref}(t) = \frac{F_0}{k - m(2\pi\phi_0)^2}(\cos(2\pi\phi_0)t - \cos(2\pi\phi_n)t), \quad (28)$$

where F_0 is the amplitude of the Lift force F_L, confirmed that the most energetic oscillation frequency corresponds to the shedding frequency associated with the cylinder case, $\phi_0 = 6.39 \times 10^{-1}$Hz, which translates to a St number of $\mathrm{St}(\phi_0) = 0.196$, as shown in Fig. 17.

Moreover, Fig. 17 highlights a strong agreement between

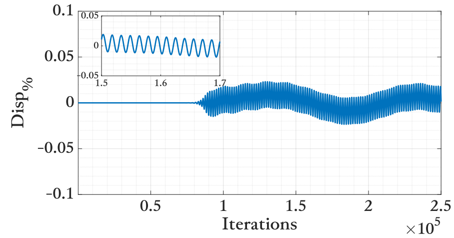

FIG. 16. Percentage displacement of the cylinder along the y-direction

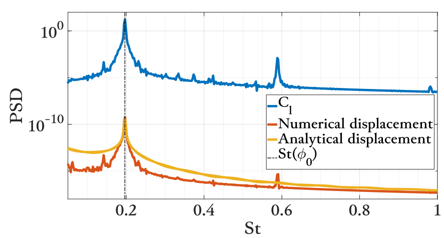

FIG. 17. Comparison between the C_l, the numerical and the analytical displacement versus St obtained with the present algorithm

the amplitude of the numerical and analytical displacement spectra, particularly at vortex shedding frequency, further confirming the validity of the simulation.

V. CONCLUSIONS

In this paper, we propose an innovative 2D algorithm that integrates the IBM with the LBM to deal with fluid structure interaction problems efficiently and with low computational cost. Notably, the algorithm achieves approximately 35 million lattice updates per second (MLUPs) using only OpenMP parallelization directives on a laptop equipped with 12 cores.

Using the IBM, forces acting on solid structures are accurately calculated. By applying Newton's third law, these forces are then transferred to adjacent fluid nodes and incorporated into the LBM using Guo's forcing scheme. This setup enables the computation of both Lift and spring forces to determine obstacle displacement.

The validation on the cylinder test case results aligns well with existing literature in terms of Drag and Lift coefficients and Strouhal number, showing errors less than 3%. The high-frequency resolution achieved by this algorithm enables precise prediction of the vortex shedding frequency and the effects of nonlinear interactions between wake-shed vortices on both Lift and Drag.

In a test case involving a cylinder-plate configuration, the algorithm reveals notable modifications in the wake structure and flow separation point. The cylinder-plate setup results in a reduced Drag coefficient compared to the cylinder alone.

Finally, a preliminary application to VIV phenomena demonstrates a higher resolution of the cylinder displacement around the original position due to Lift forces, indicating the algorithm's potential for assessing VIV dynamics. Further analyses will be carried out in future works to investigate more complex scenarios, such as the roto-translational motion studied in [64, 65] in conjunction with the VIV phenomena.

[1] Z. Alan Wei and Z. Charlie Zheng, Journal of Fluids Engineering **140**, 011105 (2018).
[2] J. M. Ramirez, Energy Conversion and Management **249**, 114852 (2021).
[3] M. Hamlehdar, A. Kasaeian, and M. R. Safaei, Renewable Energy **143**, 1826 (2019).
[4] J. Zhu, B. Ren, P. Dong, and W. Chen, Ocean Engineering **272**, 113792 (2023).
[5] H. Zhu and Y. Gao, Energy **165**, 1259 (2018).
[6] P. J. Mucha, S.-Y. Tee, D. A. Weitz, B. I. Shraiman, and M. P. Brenner, Journal of fluid mechanics **501**, 71 (2004).
[7] M.-C. Hsu and Y. Bazilevs, Computational Mechanics **50**, 821 (2012).
[8] A. Cunningham, Jr, in *29th AIAA, Fluid Dynamics Conference* (1998) p. 2423.
[9] X. He, Q. Guo, Y. Xu, L. Feng, and J. Wang, Journal of Fluid Mechanics **954**, A34 (2023).
[10] G. Falcucci, G. Amati, P. Fanelli, V. K. Krastev, G. Polverino, M. Porfiri, and S. Succi, Nature **595**, 537 (2021).
[11] G. Falcucci, G. Polverino, M. Porfiri, G. Amati, P. Fanelli, V. K. Krastev, and S. Succi, Nature **603**, E26 (2022).
[12] G. Falcucci, G. Amati, G. Bella, A. L. Facci, V. K. Krastev, G. Polverino, S. Succi, and M. Porfiri, Physical Review Letters **132**, 208402 (2024).
[13] A. L. Facci, M. Porfiri, and S. Ubertini, Journal of Fluids and Structures **66**, 36 (2016).
[14] A. Korobkin, in *Advances in Fluid Mechanics* (1996) pp. 323–371.
[15] P. Crosetto, P. Reymond, S. Deparis, D. Kontaxakis, N. Stergiopulos, and A. Quarteroni, Computers & Fluids **43**, 46 (2011).
[16] M. Bukač, S. Čanić, R. Glowinski, J. Tambača, and A. Quaini, Journal of Computational Physics **235**, 515 (2013).
[17] F. Guglietta, M. Behr, L. Biferale, G. Falcucci, and M. Sbragaglia, Soft Matter **16**, 6191 (2020).
[18] H. Zhang and W. Shi, Ocean Engineering **122**, 162 (2016).
[19] M. Zhang and J. Wang, Journal of Sensors **2016**, 2673292 (2016).
[20] H. Zhu, T. Tang, H. Zhao, and Y. Gao, Physics of Fluids **31** (2019).
[21] C. Wang, H. Tang, F. Duan, and C. Simon, Journal of Fluids and Structures **60**, 160 (2016).
[22] L. H. Feng and J. J. Wang, Journal of Fluid Mechanics **662**, 232 (2010).
[23] G.-P. Cui and L.-H. Feng, Experimental Thermal and Fluid Science **141**, 110787 (2023).

[24] E. Taheri, M. Zhao, and H. Wu, Physics of Fluids **35** (2023).
[25] H. Zhu and Y. Gao, Journal of Fluids and Structures **74**, 469 (2017).
[26] H. Zhu and Y. Gao, Ships and Offshore Structures **13**, 119 (2018).
[27] T. Krüger, H. Kusumaatmaja, A. Kuzmin, O. Shardt, G. Silva, and E. M. Viggen, *The Lattice Boltzmann Method: Principles and Practice* (Springer, 2016).
[28] J. Wu and C. Shu, Journal of Computational Physics **228**, 1963 (2009).
[29] Y. Cheng, L. Zhu, and C. Zhang, Communications in Computational Physics **16**, 136 (2014).
[30] I. Cheylan, J. Favier, and P. Sagaut, Physics of Fluids **33** (2021).
[31] S. Gsell, U. d'Ortona, and J. Favier, Physical Review E **100**, 033306 (2019).
[32] Y. Hu, H. Yuan, S. Shu, X. Niu, and M. Li, Computers & Mathematics with Applications **68**, 140 (2014).
[33] R. Benzi, S. Succi, and M. Vergassola, Physics Reports **222**, 145 (1992).
[34] X. He and L.-S. Luo, Physical review E **56**, 6811 (1997).
[35] S. Succi, *The Lattice Boltzmann Equation for Fluid Dynamics and Beyond* (Oxford University Press, 2001).
[36] P. L. Bhatnagar, E. P. Gross, and M. Krook, Physical review **94**, 511 (1954).
[37] A. Mohamad and A. Kuzmin, International Journal of Heat and Mass Transfer **53**, 990 (2010).
[38] Z. Guo, C. Zheng, and B. Shi, Physical review E **65**, 046308 (2002).
[39] C. S. Peskin, Acta numerica **11**, 479 (2002).
[40] Z.-G. Feng and E. E. Michaelides, Journal of computational physics **195**, 602 (2004).
[41] S. K. Kang and Y. A. Hassan, International Journal for Numerical Methods in Fluids **66**, 1132 (2011).
[42] R. Verzicco, Annual Review of Fluid Mechanics **55**, 129 (2023).
[43] G. Iaccarino and R. Verzicco, Appl. Mech. Rev. **56**, 331 (2003).
[44] A. De Rosis, S. Ubertini, and F. Ubertini, Journal of Fluids and Structures **45**, 202 (2014).
[45] A. De Rosis, G. Falcucci, S. Ubertini, and F. Ubertini, Journal of Fluids and Structures **49**, 516 (2014).
[46] F. Viola, G. Del Corso, and R. Verzicco, Physical Review Fluids **8**, 100502 (2023).
[47] R. Mittal and G. Iaccarino, Annu. Rev. Fluid Mech. **37**, 239 (2005).
[48] M. de Tullio and G. Pascazio, Journal of Computational Physics **325**, 201 (2016).
[49] M. Uhlmann, Journal of computational physics **209**, 448 (2005).
[50] Y.-H. Qian, D. d'Humières, and P. Lallemand, Europhysics letters **17**, 479 (1992).
[51] E. Vergnault, O. Malaspinas, and P. Sagaut, Journal of Computational Physics **231**, 8070 (2012).
[52] E. Vergnault, O. Malaspinas, and P. Sagaut, The Journal of the Acoustical Society of America **133**, 1293 (2013).
[53] J. Smagorinsky, Monthly weather review **91**, 99 (1963).
[54] L. Verlet, Physical review **159**, 98 (1967).
[55] M.-C. Lai and C. S. Peskin, Journal of computational Physics **160**, 705 (2000).
[56] S. Xu and Z. J. Wang, Journal of Computational Physics **216**, 454 (2006).
[57] M. Benson, P. Bellamy-Knights, J. Gerrard, and I. Gladwell, Journal of Fluids and Structures **3**, 439 (1989).
[58] P. Stoica, R. L. Moses, *et al.*, *Spectral analysis of signals*, Vol. 452 (Pearson Prentice Hall Upper Saddle River, NJ, 2005).
[59] S. Meloni, A. R. Proença, J. L. Lawrence, and R. Camussi, Journal of Fluid Mechanics **929**, A4 (2021).
[60] J. Dahl, F. S. Hover, and M. S. Triantafyllou, in *ISOPE International Ocean and Polar Engineering Conference* (ISOPE, 2008) pp. ISOPE–I.
[61] X. Niu, C. Shu, Y. Chew, and Y. Peng, Physics Letters A **354**, 173 (2006).
[62] X. He and G. D. Doolen, Physical Review E **56**, 434 (1997).
[63] M. Zhao, L. Cheng, H. An, and L. Lu, Journal of Fluids and Structures **50**, 292 (2014).
[64] Z. Xia, K. W. Connington, S. Rapaka, P. Yue, J. J. Feng, and S. Chen, Journal of Fluid Mechanics **625**, 249 (2009).
[65] H. Wan, H. Dong, and Z. Liang, in *50th AIAA Aerospace Sciences Meeting Including the New Horizons Forum and Aerospace Exposition* (2012) p. 1079.